

# Structure and chemical composition of the silicate dust around OH/IR stars<sup>\*</sup>

K. Demyk<sup>1</sup>, E. Dartois<sup>2,1</sup>, H. Wiesemeyer<sup>2</sup>, A.P. Jones<sup>1</sup>, and L. d'Hendecourt<sup>1</sup>

<sup>1</sup> IAS-CNRS, Université Paris XI, Batiment 121, 91405 Orsay Cedex, France

<sup>2</sup> IRAM, 300, rue de la Piscine, 38406 Saint Martin d'Hères, France

Received 31 May 2000 / Accepted 13 August 2000

**Abstract.** Using a radiative transfer code we have studied the dust shells of the two OH/IR stars IRAS 17004-4119 (OH344.93) and IRAS 17411-3154 (OH357). The ISO-SWS spectra of both sources exhibit deep amorphous silicate absorption bands at 9.8 and 17.5  $\mu\text{m}$  together with crystalline silicate emission bands at 33.6, 40.5 and 43  $\mu\text{m}$ . In both sources the 9.8  $\mu\text{m}$  silicate band shows a shoulder at 11.2  $\mu\text{m}$ . The amorphous silicates are mainly composed of olivine. With the adopted set of optical constants, the amount of amorphous pyroxene-type silicates participating in the absorption cannot exceed  $\sim 10\%$  of the amorphous silicate mass. The crystalline silicates are identified with enstatite, forsterite and diopside. They represent  $\sim 35\%$  and  $\sim 25\%$  of the amorphous silicate mass for IRAS 17004-4119 and IRAS 17411-3154, respectively. In these sources, the 11.2  $\mu\text{m}$  feature is attributed to the absorption of crystalline forsterite which is also observed in emission at 33.6  $\mu\text{m}$ . Water ice is observed in both objects through two bands in the covered wavelength range, in absorption (at 3.09  $\mu\text{m}$ ) and in emission (at 43  $\mu\text{m}$ ). The presence of water ice and crystalline forsterite bands, observed in emission and absorption, emphasizes the necessity, in such objects, of modelling the radiative transfer in order to interpret the overall spectra. Our results, compatible with classical silicate formation theories, may help to put some constraints on dust formation models.

**Key words:** stars: late-type – stars: individual: IRAS 17411-3154, IRAS 17004-4119 – stars: circumstellar matter – radiative transfer – infrared: stars

## 1. Introduction

Evolved stars represent the main site of dust formation in our Galaxy. Depending on their stage of evolution, the stars are oxygen-rich or carbon-rich and the dust formed in the envelopes around these stars is respectively preferentially oxygen-rich (silicates, oxides, H<sub>2</sub>O) or carbon-rich (PAHs, amorphous carbon,

*Send offprint requests to:* K. Demyk (demyk@ias.fr)

<sup>\*</sup> Based on observations with ISO, an ESA project with instruments funded by ESA Member States (especially the PI countries: France, Germany, the Netherlands and the United Kingdom) and with the participation of ISAS and NASA.

graphite). Among these stars, OH/IR stars are characterised by large mass loss rates (up to  $10^{-4} M_{\odot}/\text{yr}$ ), a thick dust shell composed of oxygen-rich dust and OH Maser emission at 1612, 1665, 1667 MHz. These objects are deeply embedded and their spectra show the 9.8  $\mu\text{m}$  silicate band in absorption (e.g. Habing 1996). In addition to the amorphous silicates observed in absorption, the dust shells of some OH/IR stars also contain a crystalline silicate component, observed in emission through the numerous bands at wavelengths  $\geq 20 \mu\text{m}$  (Cami et al. 1998, Sylvester et al. 1999). Most of these bands have been identified with the magnesium-rich crystalline silicates forsterite and enstatite (Waters et al. 1996, 1998, Cohen et al. 1999).

Part of the dust around OH/IR stars is cold enough to allow water ice to freeze onto the grain surfaces. It was first observed at 3.09  $\mu\text{m}$  (Soifer et al. 1981, Eiroa et al. 1983, Smith et al. 1988) and 6.0  $\mu\text{m}$  (Soifer et al. 1981). Omont et al. (1990) detected the 44  $\mu\text{m}$  band of crystalline water ice in emission. The libration mode at  $\sim 11\text{--}13 \mu\text{m}$  has been proposed to explain the shoulder observed at  $\sim 11.2 \mu\text{m}$  in the 9.8  $\mu\text{m}$  silicate band (Soifer et al. 1981, Roche & Aitken 1984). However Smith & Herman (1990) contest this identification and proposed that partially annealed (crystalline) silicates could be responsible for this feature.

We present in this article a study of the dust around the two OH/IR stars IRAS 17004-4119 (OH344.93) and IRAS 17411-3154 (OH357). The observations and the data reduction technique are described in Sect. 2. We have modelled the spectral energy distribution (SED) of the two stars using a radiative transfer code described in Sect. 3. In Sect. 4, we present our results and discuss the identification of the observed bands with different dust components. Finally, we discuss how these identifications can put some constraints on models of dust formation in Sect. 5

## 2. Observations and data reduction

The SWS spectra of IRAS 17004-4119 and IRAS 17411-3154 (hereafter IRAS 17004 and IRAS 17411) were measured with the ISO Short Wavelength Spectrometer (SWS) (de Graauw et al. 1996) in AOT01 mode, speed 2 (TDT 28901123 and 13601695 respectively). The data were processed using the standard SWS Interactive Analysis (IA) procedures (de Graauw et al. 1996) and the calibration files available in November 1999. We started the data reduction from the Standard Processed Data

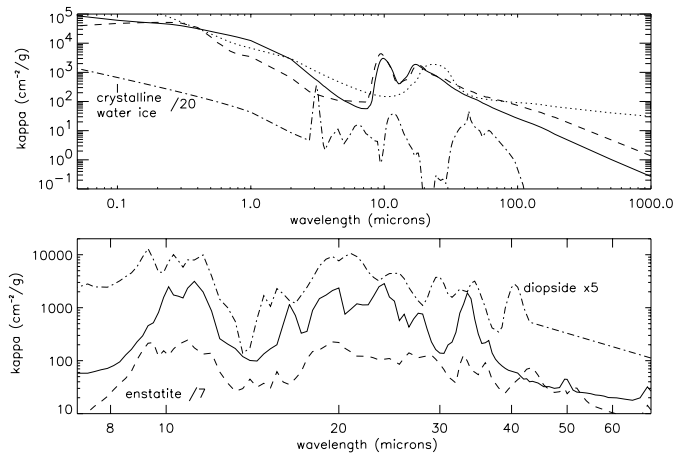


**Fig. 1.** Mass absorption coefficient for the dust species used in the model. Upper panel: amorphous olivine (continuous line), amorphous pyroxene (dashed line), FeO (dotted line) (from the Jena Group database, see text) and crystalline water ice (dotted-dashed line) (Schmitt et al. 1998), shown over the complete wavelength range used in the model. Lower panel: crystalline silicates, forsterite (continuous line), enstatite (dashed line), diopside (dotted-dashed line) shown in the 7–70  $\mu\text{m}$  wavelength range, where the vibrational bands arise.

(SPD). For both sources up and down scans were processed separately. The 7–12  $\mu\text{m}$  and 27–45  $\mu\text{m}$  ranges in IRAS 17411 exhibit memory effects similar to those described by Sylvester et al. (1999). This affects the overall flux level of the up and down scans but not the observed spectral features (at 11.2, 33.6, 40.5 and 43  $\mu\text{m}$ ) nor the band/continuum ratio. The uncertainty in the continuum flux level induced by these effects is of the order of a few% ( $\sim 3$ –10% depending on the wavelength). Because we are mostly interested in this study in the emission bands and in the band/continuum ratio, no attempt was made to correct this problem (see Sylvester et al. 1999). IRAS 17004 has a lower flux level than IRAS 17411 and thus its spectrum is much less affected by memory effects. The LWS spectrum of IRAS 17411 was measured using the LWS AOT01 (TDT 46901615) and was reduced using the LWS off-line processing software (version 7.0).

### 3. Modelling

#### 3.1. Radiative transfer modelling

We have modelled the SED of the two sources with the radiative transfer code described in Dartois et al. (1998). The model assumes a spherical symmetry with the central star being surrounded by a spherical dust shell. The input parameters are the density law, the effective temperature of the central star, the condensation temperature of the dust and the mass of the dust envelope. The inner radius of the dust shell is the radius at which the temperature is equal to the condensation temperature of the dust. The outer radius is derived from the envelope mass and the density law. The adopted effective temperature for the stars is 1800 K, typical of this kind of objects (e.g. Lorenz-Martins & de Araújo 1997). We use a density law  $n(r) \propto r^{-\beta}$  with  $\beta = 2$ ,

corresponding to a constant mass loss rate. Lorenz-Martins & de Araújo 1997 adopted a density law with  $\beta \geq 2$ , consistent with a mass-loss increasing in time, for the two studied objects and more generally for thick envelopes.  $\beta$  is difficult to constrain since increasing its value in the model does not greatly change the shape of the overall spectra. It does not change the composition of the amorphous dust inferred from the model and only leads to a slight underestimation of the crystalline silicate abundances. We adopt 900 K for the condensation temperature of the silicate dust. The resulting spectra do not strongly depend on this parameter and the model cannot be used to constrain its value. Therefore the adopted value should not be used to predict the physical structure of the newly formed dust. Crystalline water ice is incorporated in the model when the temperature in the outer parts of the envelope drops below 110 K. We have not taken into account interstellar extinction in this study. The envelopes around both objects are so dense that interstellar extinction will have negligible effects. A rapid estimation, using the normalised extinction curve from Draine & Lee (1984), shows that the spectra are not altered for column densities of interstellar matter up to  $N_H = 10^{22} \text{ cm}^{-2}$ .

The dust species incorporated into the model are amorphous olivine ( $\text{MgFeSiO}_4$ ), “cosmic” pyroxene (Mg 28.1%, Fe 17.3%, Al 1.1%, Ca 2.2%, Si 51.3%), iron oxide (FeO) (we assume the optical constants of the Jena Group, Jäger et al. 1994, Dorschner et al. 1995, Begemann et al. 1995), crystalline water ice at 60 K (Schmitt et al. 1998) and laboratory spectra of crystalline forsterite ( $\text{Mg}_2\text{SiO}_4$ ), enstatite ( $\text{MgSiO}_3$ ) and diopside ( $\text{CaMgSi}_2\text{O}_6$ ) (see Fig. 1). The laboratory spectra of forsterite, enstatite and diopside were measured at the IAS with a FT spectrometer (Bruker IFS66V), in the 2–50  $\mu\text{m}$  range, at a resolution comparable to the ISO observations. We used the standard pellet technique. Pellets were made using few tenths of a mg of the mineral powder (of submicron size particles) and 300 mg of CsI, pressed under a pressure of 10 tons to form the pellet. We derive the mass absorption coefficient from the measured transmittance spectra ( $T$ ) with the following formula:

$$\kappa = -\frac{\pi r^2}{m} \times \ln(T)$$

where  $r$  is the radius of the pellet and  $m$  the mass of mineral in the pellet. The mass absorption coefficients of the crystalline minerals were extrapolated at wavelengths  $\leq 2 \mu\text{m}$  and  $\geq 70 \mu\text{m}$  and were set equal to that of amorphous olivine. The amorphous olivine contains iron, which absorbs in the NIR, whereas the crystalline silicates do not. However, this does not influence the resulting NIR opacity or the strength of silicate bands.

#### 3.2. Dust modelling

We have modelled the absorption of iron oxide (FeO) with a continuous distribution of ellipsoids (CDE) (see Bohren & Huffman 1983). The spectra of crystalline forsterite, enstatite and diopside are laboratory spectra. The natural mineral powders used to measure the infrared spectra have an intrinsic distribution of size and shape and the comparison of laboratory spectra

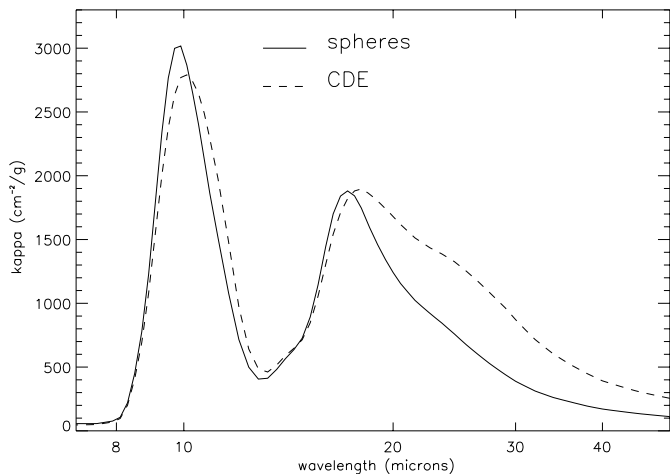


**Fig. 2.** Comparison of the mass absorption coefficient of a MRN distribution of spheres with grain sizes between 0.01 and 0.5  $\mu\text{m}$  and a continuous distribution of ellipsoids (CDE). The grains are composed of olivine:  $\text{MgFeSiO}_4$  (data from the Jena Group database, see text).

with spectra calculated from optical constants shows that they resemble spectra calculated with a CDE distribution. Discrepancies observed between the two may originate from the KBr or CsI matrix effects, deviation from the CDE distribution and/or possible agglomeration effect in the pellets (e.g. Henning & Mutschke 2000). Incorporating water ice in the form of grains (spherical or with a CDE distribution) or as a grain mantle (i.e. coated grains) has little effect on the shape of the bands, we thus used spherical grains.

For the amorphous silicates we have tested spherical grains with a MRN size distribution (Mathis et al. 1977), with grain sizes between 0.01 and 0.5  $\mu\text{m}$ , and grains with a CDE distribution. Using spherical grains or a grain population with a CDE distribution has several effects on the resultant spectra because the shape of the silicate bands and their relative intensities with respect to the continuum vary (Fig. 2). In the case of a CDE distribution, the 9.8  $\mu\text{m}$  band is broadened and shifted from 9.8 to 10.1  $\mu\text{m}$ . The 17.5  $\mu\text{m}$  band is more pronounced and shifted from 17.5 to 18  $\mu\text{m}$ . At long wavelengths ( $\lambda \geq 20 \mu\text{m}$ ) the CDE distribution absorbs more than the spheres. It appears from our results that models using a CDE distribution better fit the FIR range of both spectra. It also better fits the 9.8  $\mu\text{m}$  band of IRAS 17004 (the observed and modelled spectra are indistinguishable) but is too large for the 9.8  $\mu\text{m}$  band of IRAS 17411 which is better fitted by spheres (Fig. 3). Indeed, the comparison of the 9.8  $\mu\text{m}$  band of the two sources shows that this band is larger in IRAS 17004 than in IRAS 17411. However the width difference between the bands in the two stars is certainly a composition effect since it appears very unlikely that in one source the grains are spherical whereas they have a CDE distribution in the other. The CDE distribution considers that all shapes are equally probable. As pointed out by Ossenkopf et al. (1992) a more realistic shape distribution could be one that favors the spherical case and rejects extreme shapes like flat discs or needles. Using either spherical grains or a shape distribu-

tion does not modify our results in terms of relative abundances (of crystalline versus amorphous silicates and pyroxenes versus olivines). Therefore, in the following, we will present results for a population of spherical amorphous grains with a MRN size distribution with  $a_{\text{min}}=0.005 \mu\text{m}$  and  $a_{\text{max}}=0.5 \mu\text{m}$ .

## 4. Results

The observed and modelled spectra are shown in Fig. 3. The overall shape of the SED of both sources, the emission bands at long wavelength and the shape of the 9.8  $\mu\text{m}$  band are reasonably well reproduced by the modelled spectra. However, some discrepancies between the fits and the observed spectra can be seen. In particular the near infrared (NIR) opacity at wavelength  $\leq 7 \mu\text{m}$  is not accounted for, the far infrared (FIR) flux is too low and the emission in the 15–30  $\mu\text{m}$  range is overestimated by the model. In the following we discuss these differences. We also discuss the composition of the dust in the shell inferred from the different spectral features: the 9.8  $\mu\text{m}$  band and the shoulder at 11.2  $\mu\text{m}$ , the emission bands at 33.6, 40.5 and 43  $\mu\text{m}$  and the water ice bands at 3.09 and 43  $\mu\text{m}$ . Note that in the following, the percentages are relative to the amorphous silicate mass and not to the total (amorphous plus crystalline) silicate mass.

### 4.1. The NIR opacity

The NIR opacity in the 2–7  $\mu\text{m}$  wavelength range is not properly reproduced by the modelled spectra. There could be several origins for this, such as scattering effects that are not well accounted for in the model, missing dust species that absorb or scatter in this wavelength range, or geometrical effects.

According to Bedijn (1987), for a grain size of 0.1  $\mu\text{m}$ , scattering has no effect on the spectral shape for wavelengths greater than 2 and 2.8  $\mu\text{m}$ , for optical depths at 9.7  $\mu\text{m}$  of 4 and 30 respectively ( $\tau_{9.8 \mu\text{m}} \sim 10$  for both sources). However, this may not be true for larger grain sizes. Lorenz-Martins & de Araújo (1997) achieve a fit the NIR opacity of IRAS 17004 and IRAS 17411 with 0.7  $\mu\text{m}$  and 0.85  $\mu\text{m}$  diameter grains, respectively. We obtain the best fits to the spectra with a population of grains with a MRN size distribution from 0.005 to 0.5  $\mu\text{m}$  (Fig. 3). Increasing the grain size actually improves the fits in the NIR but does not entirely account for the 2–8  $\mu\text{m}$  wavelength range opacity. Although scattering is incorporated into the model via the extinction efficiency, it is not explicitly taken into account in the radiative transfer calculations. A proper treatment of the scattering could help to explain the discrepancy between the observed and modelled NIR opacity.

Another possibility to account for the NIR opacity would be to add different dust components (iron oxide, graphite, water ice) to the amorphous and crystalline silicates. An admixture of iron oxide (FeO) and metallic iron, which strongly absorb in the NIR range, increases the resultant opacity and improves the fit. The amount of iron that can be added in the model is limited by cosmic abundance constraints. Depending on the authors, the amount of iron (by atomic number) in the solid phase is similar to the amount of silicon (Savage & Sembach 1996) or is 50% more

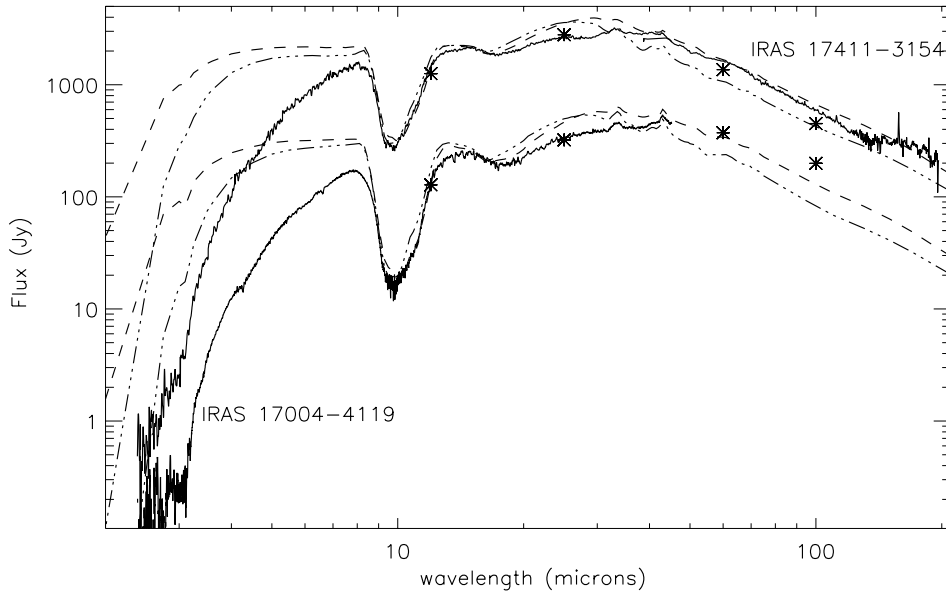


**Fig. 3.** Best fit to the spectra of the two OH/IR stars for a MRN size distribution with  $a_{min} = 0.005 \mu\text{m}$  and  $a_{max} = 0.5 \mu\text{m}$  (dotted-dashed lines) and a grain population with a CDE distribution (dashed lines). For IRAS 17004-4119: amorphous olivine ( $\text{MgFeSiO}_4$ ), 20% FeO, crystalline forsterite (15%), enstatite and diopside (10% each) and crystalline water ice. For IRAS 17411-3154: amorphous olivine ( $\text{MgFeSiO}_4$ ), 20% FeO, crystalline forsterite (5%), enstatite and diopside (10% each) and water ice. The stars represent the IRAS measurements.

abundant than silicon (Snow & Witt 1996). Then, assuming that all the silicon in the solid phase is in silicates, one can add an amount of iron up to 50% of the amorphous olivine ( $\text{MgFeSiO}_4$ ) concentration if we adopt the Snow & Witt abundances. This is still not enough to reproduce the strong observed NIR opacity. The water ice opacity falls by  $\sim 4$  orders of magnitude between 3 and  $1 \mu\text{m}$  and thus cannot account for the extra NIR opacity. This is confirmed by the results of the model. The addition of graphite ( $\sim 20\%$  by mass, relative to the amorphous silicates) can fit the NIR opacity (Demyk et al. 2000). However graphite is not expected to form in oxygen-rich environments and it is difficult to justify the presence of such a large mass of carbon-rich dust around OH/IR stars. One can argue that these stars are at the end of their oxygen-rich phase and are at the transition toward the carbon-rich phase. Duari et al. (1999) predict that some carbon-rich molecules can be produced in the envelopes around Mira variable stars. Some of these molecules have been observed in the radio range (HCN, CS) and with ISO ( $\text{CO}_2$ ) (Duari et al. 1999). However, graphite is the end-product of the dust formation around carbon-rich stars and it is unlikely that it could have been formed even if the objects were transition objects.

#### 4.2. The $11.2 \mu\text{m}$ feature

An additional absorption feature in the  $9.8 \mu\text{m}$  silicate band, at  $\sim 11.2\text{--}11.5 \mu\text{m}$ , is observed in several OH/IR stars (Soifer et al. 1981, Roche & Aitken 1984). In these sources the  $3.09 \mu\text{m}$  feature of water ice is also present and the shoulder of the silicate band was identified with the libration mode of water ice. However, Smith & Herman (1990) contest this identification considering that some sources have a strong water ice band at  $3.09 \mu\text{m}$  but no detectable libration mode. Furthermore they observed this shoulder in OH138.0+7.3 which does not show any absorption at  $3.09 \mu\text{m}$ . They proposed that the feature could be due to crystalline silicates. Sylvester et al. (1999) observed this

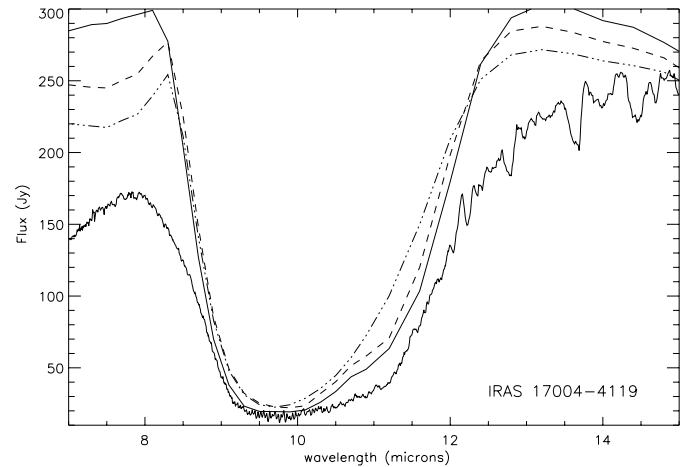


**Fig. 4.** Best fit to the  $9.8 \mu\text{m}$  silicate band in IRAS 17004. Continuous line: amorphous olivine, crystalline forsterite (15%), enstatite and diopside (10% each) and crystalline water ice; dashed line: amorphous olivine and 15% of crystalline forsterite; dotted-dashed line: amorphous olivine and crystalline water ice.

feature in the ISO-SWS spectra of several OH/IR stars, including IRAS 17411 (AFGL5379), and found that the feature does not clearly correlate with the water ice bands.

This shoulder is also present in the IRAS-LRS spectra of both sources. In their ISO spectra, the feature is clearly present in the up and down scans. In the case of spherical amorphous grains, the silicate band of IRAS 17004 is well-fitted by a grain population containing amorphous olivine with  $\sim 10\%$  of crystalline enstatite,  $\sim 10\%$  of diopside and  $\sim 15\%$  of crystalline forsterite with or without water ice (Fig. 4). The band in IRAS 17411 is reproduced with amorphous olivine and  $\sim 5\%$  of crystalline forsterite,  $\sim 10\%$  of crystalline enstatite and  $\sim 10\%$  of diopside with or without water (Fig. 5). The crystalline silicate components allow us to fit *simultaneously* the  $9.8 \mu\text{m}$  band, including the  $11.2 \mu\text{m}$  feature, *and* the emission bands at longer

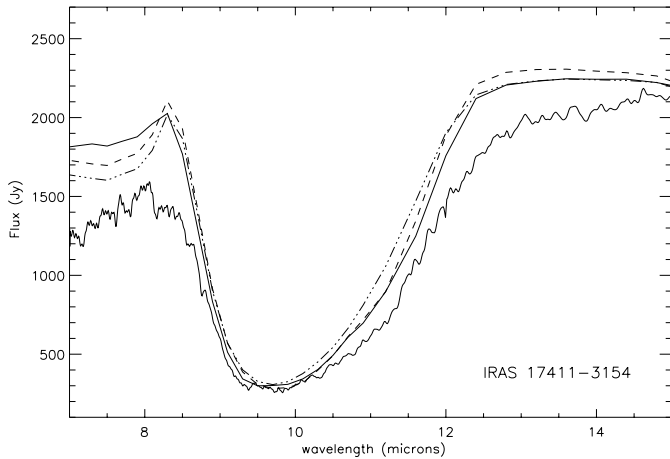


**Fig. 5.** Best fit to the  $9.8 \mu\text{m}$  silicate band in IRAS 17411. Continuous line: amorphous olivine, crystalline forsterite (5%), enstatite and diopside (10% each) and crystalline water ice; dashed line: amorphous olivine and 5% of crystalline forsterite; dotted-dashed line: amorphous olivine and crystalline water ice.

wavelengths (see e.g. Fig. 9). In both sources, adding water ice in quantities such that it fits the  $43 \mu\text{m}$  band does not change the  $10 \mu\text{m}$  silicate band because the libration mode of water ice is not detectable. Models with only amorphous olivine and crystalline forsterite reproduce the observed shoulder but the band is too narrow and the addition of crystalline pyroxenes (enstatite and diopside) is necessary to account for the width of the band.

#### 4.3. Water ice

In optically thick oxygen-rich environments around OH/IR stars, water ice is expected to freeze onto the surface of the newly formed refractory grains (see Sylvester et al. 1999). The spectra of both sources show an emission band at  $43 \mu\text{m}$  which is attributed to the emission of crystalline pyroxene-type refractory grains and to crystalline water ice emission. In the models, the strength of this band is very sensitive to the amount of water ice and allows us to constrain it better than the other water ice bands. Although the  $2\text{--}3 \mu\text{m}$  spectral region is very noisy, both sources also show an absorption band at  $3.09 \mu\text{m}$ , identified with water ice absorption. At  $6 \mu\text{m}$  the spectra of both objects show an inflection but its identification is less clear and the band could be due to absorption from water ice as well as gaseous water. The  $3.09 \mu\text{m}$  and  $6 \mu\text{m}$  bands can be tentatively fitted by crystalline water ice rather than amorphous water ice (see Fig. 6). From the saturated  $3.09 \mu\text{m}$  band we can derive a lower limit to the water ice abundance and an upper limit from the  $6 \mu\text{m}$  band. We find a column density for the water ice of  $9\text{--}35 \times 10^{17} \text{ cm}^{-2}$  and  $7\text{--}33 \times 10^{17} \text{ cm}^{-2}$  respectively for IRAS 17004 and IRAS 17411 (with the absorption cross-section of pure water ice from Gerakines et al. 1995). The wide range we find can partly be explained by the noisy spectra in the  $3 \mu\text{m}$  region and because the upper limit is certainly overestimated due to the presence of gaseous water around  $6 \mu\text{m}$ . However these estimations are in

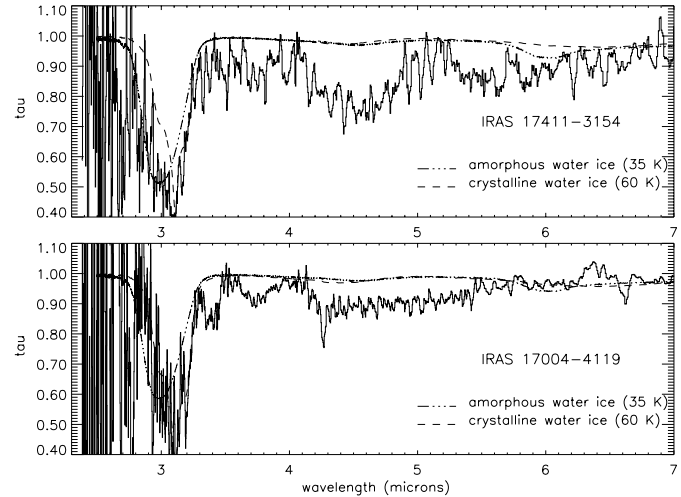


**Fig. 6.** Water ice bands in the NIR wavelength range. The estimated continuum has been subtracted for each source. Absorption caused by spherical grains of amorphous and crystalline water ice are shown. The optical constants are from Schmitt et al. (1998).

agreement with the column density of  $1.12 \times 10^{18} \text{ cm}^{-2}$  derived by Sylvester et al. (1999) for IRAS 17411.

#### 4.4. Composition of the amorphous silicates

Because amorphous silicate bands are broad and structureless it is difficult to study the chemical composition of these silicates. To compare the dust features between different astronomical objects, some authors derived the optical constants of the dust from the spectra of specific objects (e.g. the “astronomical silicate” from Draine & Lee (1984), David & Pégourié (1995), Ossenkopf et al. (1992)). However these optical constants are usually not interpreted in terms of a given composition. The goal of the work presented here is to study the structure of the dust around these two evolved stars and also to put some constraints on the chemical composition of the crystalline and amorphous dust. Thus, in the model, we decided to use laboratory data on dust analogues of known composition and structure.

In both sources, the  $9.8 \mu\text{m}$  band is well-fitted by amorphous olivine-type silicates. This is also the case for the dust around evolved stars (OH/IR stars, Mira stars...) and in the ISM (Dorschner et al. 1988). However around protostars, the silicate band peaks at slightly shorter wavelengths ( $9.6 \mu\text{m}$ ) than around evolved stars and the dust is identified with pyroxene-type silicates (Jäger et al. 1994, Dorschner et al. 1995, Demyk et al. 1999) or with a mixture of olivine and pyroxene (Malfait et al. 1999). We have thus searched for amorphous pyroxenes in the spectra of these two stars. Fig. 7 and 8 present the effect of incorporating different amounts of amorphous pyroxene, in addition to the olivine, on the  $9.8 \mu\text{m}$  band of IRAS17004 and IRAS 17411 respectively. The Si-O stretching mode in pyroxenes peaks at shorter wavelengths than in olivine and clearly does not fit the spectrum. No good fit to the  $9.8 \mu\text{m}$  band can be achieved with more than 10% of amorphous pyroxene (by mass, relative to the total amorphous silicate mass).

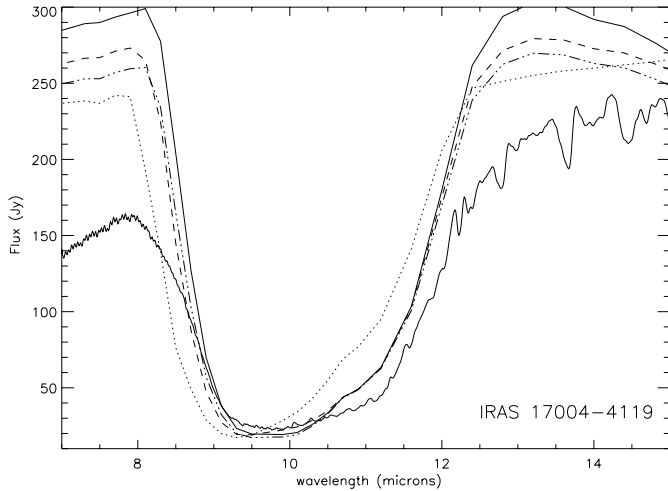


**Fig. 7.** Amount of amorphous pyroxene present in the dust shell around IRAS 17004 for spherical grain of  $0.1 \mu\text{m}$ . Relative quantity of amorphous pyroxene versus amorphous olivine: 1:0 (dotted line), 0.2:0.8 (dashed line), 0.1:0.9 (dotted-dashed line), 0:1 (continuous line).

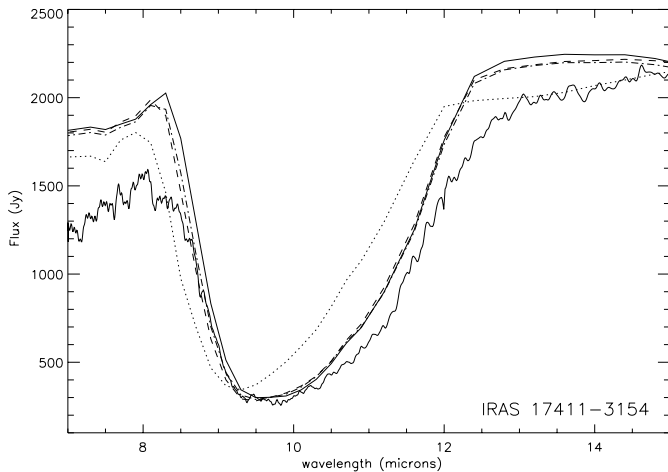


**Fig. 8.** Amount of amorphous pyroxene present in the dust shell around IRAS 17411 for spherical grain of  $0.1 \mu\text{m}$ . Relative quantity of amorphous pyroxene versus amorphous olivine: 1:0 (dotted line), 0.2:0.8 (dashed line), 0.1:0.9 (dotted-dashed line), 0:1 (continuous line).

#### 4.5. Composition of the crystalline silicates

The composition of the crystalline silicates is constrained by their numerous vibrational bands observed in emission at long wavelengths. Forsterite ( $\text{Mg}_2\text{SiO}_4$ ) is responsible for the  $33.6 \mu\text{m}$  band. The peak positions of the olivine bands are sensitive to the Mg/Fe ratio (Koike et al. 1993). This dependence allows us to constrain the amount of iron contained in the crystalline olivine. In both sources we find that the crystalline olivine is magnesium rich with no more than 10% of iron. This result is in agreement with previous works (e.g. Molster et al. 1999). Several possible explanations for this are discussed by Tielens et al. (1998) and Nuth et al. (2000). Crystalline pyroxenes explain the bands at  $40.5$  and  $43 \mu\text{m}$ . Enstatite ( $\text{MgSiO}_3$ ) participates in the  $43 \mu\text{m}$  band together with crystalline water ice (Fig. 9)

while diopside ( $\text{CaMgSi}_2\text{O}_6$ ) explains the  $40.5 \mu\text{m}$  band. The crystalline silicates that give the best fit to the spectra are  $\sim 15\%$  forsterite,  $\sim 10\%$  enstatite and  $\sim 10\%$  diopside for IRAS 17004 and  $\sim 5\%$  forsterite,  $\sim 10\%$  enstatite and  $\sim 10\%$  diopside for IRAS 17411. With these quantities of crystalline minerals, both the  $9.8 \mu\text{m}$  band and the emission bands are well fitted. The band/continuum ratio is well reproduced for the three bands at  $33.6$ ,  $40.5$  and  $43 \mu\text{m}$  but the modelled spectra do not correctly reproduce the observed underlying continuum at wavelengths greater than  $20 \mu\text{m}$ . In the modelled spectra, the dust emits too much in the  $20\text{--}30 \mu\text{m}$  region, whereas at longer wavelength it absorbs too much. Thus the dust temperature calculated in the model seems too high. This may be due to spatial distribution effects not taken into account in the model. Part of the dust may be colder due to the presence of a detached dust shell or of a disk. Such complex structure has been observed in the envelope around IRC+10216 (Mauron & Huggins 1999).

We have searched, in the spectra, for other types of silicates predicted to form around these stars such as spinel ( $\text{MgAl}_2\text{O}_4$ ) and melilite ( $\text{Ca}_2\text{Al}_2\text{SiO}_7$ ). Crystalline melilite has three strong vibrational bands at  $\sim 10$ ,  $23.9$  and  $36.2 \mu\text{m}$  which are not observed in the spectra. The maximum amount of melilite that could be present in both sources is constrained by the low abundance of melilite, about 2% (determined by the abundance of Ca relative to Si) rather than by the presence of the bands in the spectra since they are not detectable if 2% of melilite is incorporated into the model. Amorphous melilite and, more generally, amorphous aluminosilicates cannot be present around these stars for the same reasons as the amorphous pyroxenes (the stretching mode peaks at too short a wavelength and cannot reproduce the observed  $9.8 \mu\text{m}$  band). Spherical grains of spinel have been proposed to explain the  $13 \mu\text{m}$  feature observed in emission in the spectra of some O-rich AGB stars and possibly another band at  $16.8 \mu\text{m}$  (Posch et al. 1999). Spherical grains of spinel have two strong vibrational bands at  $12.95$  and  $16.8 \mu\text{m}$ . These bands are not present in the spectra of the two sources and less than 1–2% of spherical grains of spinel could be hidden in the spectra. If we adopt a CDE distribution instead of spherical grains, the two bands broaden and up to 5–7% of spinel could be present in both sources. However, according to Posch et al. (1999), a CDE distribution does not reproduce the two observed bands.

## 5. Discussion

A precise knowledge of the composition and structure of the dust around evolved stars will place some constraints on its formation and on the physical environment in the shell. According to the thermodynamic condensation sequence at equilibrium, two branches exist (Table 1, Tielens et al. 1998). The first condensation products are aluminium oxide ( $\text{Al}_2\text{O}_3$ ) or titanium oxide ( $\text{TiO}_2$ ) which provide the seeds for further condensation processes. The first branch describes the condensation of forsterite ( $\text{Mg}_2\text{SiO}_4$ ), probably on the  $\text{Al}_2\text{O}_3$  or  $\text{TiO}_2$  grains, followed by the formation, through gas-solid reactions, of enstatite ( $\text{MgSiO}_3$ ) and eventually fayalite ( $\text{Fe}_2\text{SiO}_4$ ). In the second branch, aluminium oxide reacts with the gas to form

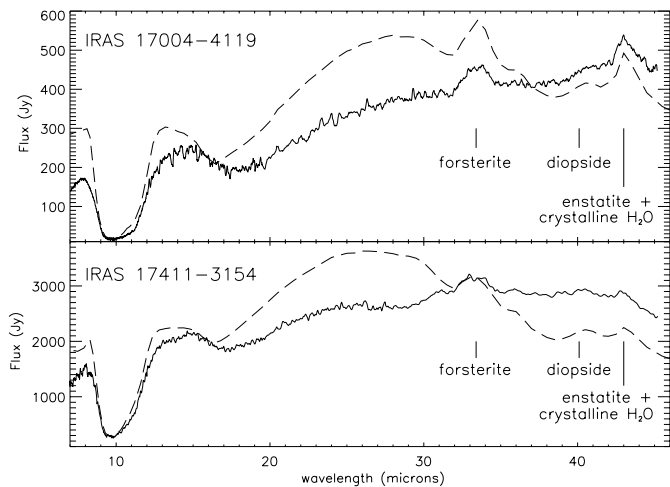


**Fig. 9.** Best fits to the crystalline silicate emission bands. The dust composition is amorphous olivine, iron oxide, crystalline water ice, crystalline enstatite, forsterite and diopside. See text for the relative abundance of each dust component in the two sources.

melilite ( $\text{Ca}_2\text{Al}_2\text{SiO}_7$ ) and finally diopside ( $\text{CaMgSi}_2\text{O}_6$ ) and spinel ( $\text{MgAl}_2\text{O}_4$ ). Solid-solid reactions may eventually lead to the formation of anorthite ( $\text{CaAl}_2\text{Si}_2\text{O}_6$ ) from diopside. This scenario is based on thermodynamic considerations only, and its effective completion will depend on the physical conditions in the condensation zone and on the kinetic timescale of the dust envelope compared to the reactions timescale.

Our results do not contradict this scheme. We do not see evidence for the presence of pure  $\text{Al}_2\text{O}_3$  grains. On the other hand we identify diopside in the dust shell. Thus, some of the  $\text{Al}_2\text{O}_3$  may have been the nucleation seeds for the silicate grains while the remaining  $\text{Al}_2\text{O}_3$  has followed the second branch of the LTE condensation sequence to form diopside. No evidence is found for the presence of spinel, melilite or anorthite. Thus, if this scenario is right, within the evolutionary time scale of the dust envelope, the gas-solid reactions leading to the formation of diopside efficiently convert melilite into diopside, but not into spinel, whereas solid-solid reactions cannot convert it into anorthite. The detection of enstatite shows that the first branch of the condensation sequence, the most important one in terms of abundances, takes place, at least until the formation of enstatite. The crystalline silicates in both sources are magnesium-rich and crystalline fayalite is not detected in the spectra. However, it is difficult to say if the sequence stopped before or after the formation of fayalite because amorphous fayalite, which is difficult to detect, could be present in the sources. The condensation models predict that for a gas of solar composition the enstatite/forsterite ratio is  $\sim 4$ . In both sources this ratio is  $\sim 0.1$ , much smaller than 4, indicating either that the gas does not have a solar composition and/or that the sequence stopped before the formation of fayalite.

Thus, qualitatively at least, the composition of the dust species identified in both sources is in agreement with the classical thermodynamic condensation sequence. However, these theories do not predict the structure of the newly formed dust

**Table 1.** Silicate thermodynamic condensation sequence for a gas of solar composition. From Tielens et al. (1998). Temperatures refer to the first appearance of a mineral at a pressure of  $10^{-3}$  (left) and  $10^{-10}$  atm (right). Species in *italic* are detected in the spectra.

		↓	1760-1300 K
		Corundum $\text{Al}_2\text{O}_3$	
		↓	1625-1400 K
		Melilite $\text{Ca}_2\text{Al}_2\text{SiO}_7$	
		↓	1450-1100 K
	↓	<i>Diopside</i> $\text{CaMgSi}_2\text{O}_6$	
	1440-1050 K	↓	
	<i>Forsterite</i> $\text{Mg}_2\text{SiO}_4$	Spinel $\text{MgAl}_2\text{O}_4$	
	↓	↓	1360-1000 K
	1350-1040 K	Anorthite $\text{CaAl}_2\text{Si}_2\text{O}_6$	
	<i>Enstatite</i> $\text{MgSiO}_3$		
	↓		
	1100-950 K		
	Fayalite $\text{Fe}_2\text{SiO}_4$		

↓ Direct condensation from the gas phase

↓ Gas-solid reaction

↓↓ Solid-solid reaction

which will strongly depend on the physical conditions and the kinetics of the condensation zone. ISO revealed that crystalline silicates are present in the dust shells of some evolved stars. Cami et al. (1998) and Sylvester et al. (1999) noticed that the crystalline bands are observed in the spectra of stars with high mass-loss rates, whereas low mass-loss rate stars do not exhibit these bands. However this does not necessarily mean that low-mass stars do not produce crystalline silicates since radiative transfer models show that a degree of crystallinity (mass fraction of the crystalline silicates with respect to the total mass of the silicates) of 10% or 20% will be undetectable in ISO spectra of stars with a mass-loss rate up to, respectively,  $6 \times 10^{-7}$  and  $2 \times 10^{-7} M_{\odot}/\text{yr}$  (Kemper et al. 2000). Assuming that most of the silicate grains are produced in the amorphous state (Rietmeijer et al. 1999), they must crystallise in the stellar envelopes. Sogawa & Kozasa (1999) show that silicates condensed onto  $\text{Al}_2\text{O}_3$  grains completely crystallise for stars with mass-loss rates  $\geq 3 \times 10^{-5} M_{\odot}/\text{yr}$ . However other scenarios have to be found if low mass-loss rate stars are also found to contain crystalline silicates.

In both sources, the ratio of the amorphous to the crystalline component is different for the olivines and for the pyroxenes. About 10% of the total amount of olivine is crystalline, in the form of forsterite. For the pyroxenes, if we assume that amorphous pyroxenes represent at most 10% of the amorphous silicates, then almost all the pyroxenes (65–100%, of the total pyroxene) are crystalline, in the form of enstatite and diopside. Assuming that the silicates are produced in the amorphous state this indicates that the pyroxenes are more efficiently crystallised than the olivines. Brucato et al. (1999) show that the spectra of annealed amorphous pyroxene exhibit the bands of crystalline enstatite. They derived the activation energy of the amorphous to crystalline transition for pyroxene to be 47,500 K.

On the other hand, Lenzuni et al. (1995) derived the activation energy for the amorphous to crystalline transition for Mg-SiO-H<sub>2</sub> smokes to be 41,000 K (from the experimental data of Nuth & Donn 1982). Annealing of such smokes results in crystalline forsterite and periclase (MgO) (Nuth & Donn 1982), therefore we can consider that this activation energy is characteristic of olivine. According to Table 1, forsterite and enstatite are formed at similar temperatures. The enstatite grains thus experience the same temperatures as forsterite. Thus, adopting an activation energy of 47,500 and 41,000 K for, respectively, pyroxene and olivine, the olivines will crystallise faster than the pyroxenes, in contradiction with our results.

Our results could be explained if the enstatite grains reside at higher temperatures for longer than the forsterite grains. This could be the case if we consider the following scenario. Once the forsterite grains have been formed, most of them escape rapidly from the condensation region. These grains thus stay amorphous and do not transform into enstatite because the temperature is too low. The remaining grains stay in the region of high temperature. Then these grains will crystallise, part of them to form the observed component of crystalline forsterite while the other part of the grains will react with the gas phase to form the enstatite grains before they crystallise. However, a physical mechanism responsible for this behaviour and a detailed modelling of the dust condensation and of the dust envelope kinetics are needed to verify such an hypothesis. It may also not be appropriate to compare the activation energies derived by Lenzuni et al. (1995) and Brucato et al. (1999) because the amorphous materials used are not produced with the same technique. Thus, the structure of the starting materials could be different and this could change the time needed to reach the crystallisation. It would be interesting to measure the activation energy of the amorphous to crystalline transition for amorphous olivine produced in the same way as the amorphous pyroxenes in Brucato et al. (1999).

However, the hypothesis that the dust is produced in the amorphous state may not be right and if we adopt Tielens (1998) model, one may be able to explain our results. This scenario follows the first branch of the condensation sequence. It is based on two physical considerations: the first is that the silicates are formed in a crystalline state at a temperature higher than their glass temperature and in an amorphous state at lower temperatures. The second consideration is that the reaction of enstatite with gaseous iron results in amorphous Fe-rich olivines (Tielens 1990). According to this scenario forsterite and enstatite are formed in a crystalline state and the observed crystalline forsterite and enstatite are those that escape the transformation into enstatite and the reaction with the iron, respectively. Thus this scenario is able to explain why all the pyroxenes are crystalline whereas only a small fraction of the olivines are. However, it requires that forsterite and enstatite are formed at high enough temperatures for them to be crystalline. If one adopts Brucato et al. (1999) value for the activation energy of the amorphous to crystalline transition for pyroxenes, then the glass temperature we deduce will be higher than that for olivines ( $\sim 1050$  K, Tielens 1990) by about 200 K. Then, the crystalline sil-

icates must form at a temperature higher than  $\sim 1200$  K. Thus, the temperature at which the silicates are formed appears to be the key parameter that could discriminate between these different theories. Also, a precise knowledge of the activation energies of minerals, determined in a homogeneous way would be very helpful.

## 6. Conclusion

The large wavelength coverage of the ISO data, combined with the modelling of the radiative transfer in the objects, have allowed us to determine quantitatively the composition and structure of the dust around the two OH/IR stars IRAS 17004-4119 (OH344.93) and IRAS 17411-3154 (OH357). The dust around these two stars is mainly composed of amorphous and crystalline silicates. The amorphous silicates are mostly composed of olivine-type silicates. No more than 10% of amorphous pyroxene could be present in both sources. The crystalline silicates which emit at long wavelength are forsterite (33.6  $\mu\text{m}$  band), enstatite (43  $\mu\text{m}$  band) and diopside (40.5  $\mu\text{m}$  band). They represent  $\sim 35\%$  and  $\sim 25\%$  of the amorphous silicate mass, respectively, for IRAS 17004-4119 and IRAS 17411-3154. Some oxides may be present in the dust shell: FeO improves the fit to the spectra in the NIR and Al<sub>2</sub>O<sub>3</sub> could be present as the cores of the silicate grains. Both stars exhibit a shoulder at 11.2  $\mu\text{m}$  in the 9.8  $\mu\text{m}$  band due to the absorption of crystalline forsterite, which is also observed in emission at 33.6  $\mu\text{m}$ . Crystalline water ice, observed in absorption at 3.09  $\mu\text{m}$  and in emission at 43  $\mu\text{m}$  is not sufficiently abundant to explain this shoulder.

The derived chemical composition of the dust is compatible with simple condensation models at thermodynamic equilibrium. The analysis of the dust structure shows that only  $\sim 10\%$  of the olivines are crystalline whereas almost all of the pyroxenes are crystalline ( $\sim 65\text{--}100\%$ ). The physical structure of the dust may reflect the dynamical timescales in the envelopes, from the formation of the dust to its ejection from the condensation zone. Such results may be used to constrain kinematic model of the grain nucleation and condensation in the envelopes of evolved stars.

*Acknowledgements.* We would like to thank Chiyoeko Koike for providing us the samples of forsterite and enstatite powders. We thank an anonymous referee for his comments that have greatly helped to improve this paper.

## References

- Bedijn P.J., 1987, A&A 186, 136
- Begemann B., Henning Th., Mutschke H., et al., 1995, Planet. Space Sc. 43, 1257
- Bohren C.F., Huffman D.R., 1983, In: Absorption and Scattering of Light by Small Particles. John Wiley, New York
- Brucato J.R., Colangeli L., Menella V., et al., 1999, A&A 348, 1012
- Cami J., De Jong T., Justtanont K., et al., 1998, Ap&SS 255, 339
- Cohen M., Barlow M.J., Sylvester R.J., et al., 1999, ApJ 513, L135
- Dartois E., Cox P., Roelfsema P.R., et al., 1998, A&A 338, L21
- David P., Pégourié B., 1995, A&A 293, 833
- de Graauw T., Haser L.N., Beintema D.A., et al., 1996, A&A 315, L49

- Demyk K., Jones A.P., Dartois E., et al., 1999, *A&A* 349, 267
- Demyk K., Dartois E., Wiesemeyer H., et al., 2000, In: ISO beyond the peaks: The 2nd ISO workshop on analytical spectroscopy. in press
- Dorschner J., Friedemann C., Guertler J., et al., 1988, *A&A* 198, 223
- Dorschner J., Begemann B., Henning Th., et al., 1995, *A&A* 300, 503
- Draine B.T., Lee H.M., 1984, *ApJ* 285, 89
- Duari D., Cherchneff I., Willacy K., 1999, *A&A* 341, L47
- Eiroa C., Hefele H., Qian Zhong-yu, 1983, *A&AS* 54, 309
- Gerakines P.A., Schutte W.A., Greenberg J.M., et al., 1995, *A&A* 296, 810
- Habing H.J., 1996, *A&AR* 7, 97
- Henning Th., Mutschke H., 2000, In: Sitko M.L., Sprague A.L., Lynch D.K. (eds.) *Thermal Emission Spectroscopy and Analysis of Dust, Disks and Regoliths*. p. 253
- Jäger C., Mutschke H., Begemann B., et al., 1994, *A&A* 292, 641
- Kemper F., Waters L.B.F.M., de Koter A., et al., 2000, In: ISO beyond the peaks: The 2nd ISO workshop on analytical spectroscopy. in press
- Koike C., Shibai H., Tachiyama A., 1993, *MNRAS* 264, 654
- Lenzuni P., Gail H.P., Henning Th., 1995, *ApJ* 447, 848
- Lorenz-Martins S., de Araújo F.X., 1997, *MNRAS* 291, 296
- Malfait K., Waelkens C., Bouwman J., et al., 1999, *A&A* 345, 181
- Mathis J.S., Rumpl W., Nordsieck K.H., 1977, *ApJ* 217, 425
- Mauron N., Huggins P.J., 1999, *A&A* 349, 203
- Molster F.J., Yamamura I., Waters L.B.F.M., et al., 1999, *Nat* 401, 563
- Nuth J.A., Donn B., 1982, *ApJ* 257, L103
- Nuth J.A., Rietmeijer F.J.M., Hallenbeck S.L., et al., 2000, In: Sitko M.L., Sprague A.L., Lynch D.K. (eds.) *Thermal Emission Spectroscopy and Analysis of Dust, Disk, and Regoliths*. p. 313
- Omont A., Forveille T., Moseley S.H., 1990, *ApJ* 355, L27
- Ossenkopf V., Henning Th., Mathis J.S., 1992, *A&A* 261, 567
- Posch T., Kerschbaum F., Mutschke H., et al., 1999, *A&A* 352, 609
- Rietmeijer F.J.M., Nuth J.A., Karner J.M., 1999, *ApJ* 527, 395
- Roche P.F., Aitken D.K., 1984, *MNRAS* 209, 33
- Savage B.D., Sembach K.R., 1996, *ARA&A* 34, 279
- Schmitt B., Quirico E., Grundy W.M., 1998, *Solar System Ices*, 199
- Smith R.G., Herman J., 1990, *A&A* 227, 147
- Smith R.G., Sellgren K., Tokunaga A.T., 1988, *ApJ* 334, 209
- Snow T.P., Witt A.N., 1996, *ApJ* 468, L65
- Sogawa H., Kozasa T., 1999, *ApJ* 516, L36
- Soifer B.T., Willner S.P., Rudy R.J., et al., 1981, *ApJ* 250, 631
- Sylvester R.J., Kemper F., Barlow M.J. et al., 1999, *A&A* 352, 587
- Tielens A.G.G.M., 1990, In: Mennessier M.O., Omont A. (eds.) *From Miras to Planetary Nebulae: Which Path for Stellar Evolution?* p. 186
- Tielens A.G.G.M., Waters L.B.F.M., Molster F.J., et al., 1998, *Ap&SS* 255, 415
- Waters L.B.F.M., Molster F.J., de Jong T., et al., 1996, *A&A* 315, L361
- Waters L.B.F.M., Beintema D.A., Zijlstra A.A., et al., 1998, *A&A* 331, L61